



Transient Natural Convection and Entropy Generation Analysis in a Stratified Square Enclosure

Md. Nayem Hossain¹, Syed Mehedi Hassan Shaon¹, Md. Mahafujur Rahaman^{2,3 *} 

¹ Department of Chemical Engineering, Z. H. Sikder University of Science and Technology, Shariatpur 8024, Bangladesh.

² Department of Computer Science and Engineering, Z. H. Sikder University of Science and Technology, Shariatpur 8024, Bangladesh.

³ Department of Mathematics, Jagannath University, Dhaka 1100, Bangladesh.

ABSTRACT: This study examines transient natural convection (NC) heat transfer (HT) and entropy generation (Egen) in a square enclosure containing thermally stratified water. The model considers uniform heating at the bottom wall, stratified vertical walls, and a cooled top boundary. Governing equations are addressed through the finite volume (FV) method, with simulations performed across a range of Rayleigh numbers (Ra) from 10^0 to 5×10^6 , a fixed Prandtl number (Pr) of 7.01, for water. Various physical quantities were analyzed across the spectrum of Ra to capture the complex dynamics of convective flow. This encompasses streamline and isotherm plots, the temporal evolution of temperature, phase-space representations via limit cycles and limit points, along with spectral analysis, including the average Nusselt number (Nu), local entropy generation (El), and local Bejan number (Bel). The results reveal successive bifurcations with increasing Ra: a pitchfork bifurcation ($Ra = 8 \times 10^3$ – 10^4) leads to symmetry breaking, a Hopf bifurcation ($Ra = 2 \times 10^5$ – 3×10^5) induces periodic oscillations, and chaotic flow emerges at $Ra = 10^6$ – 2×10^6 . The average Nusselt number at the bottom wall increases from 5.84 for $Ra = 2 \times 10^5$ to 15.87 for $Ra = 2 \times 10^6$, corresponding to a 171.75% enhancement in the HT. The numerical framework was validated by comparing it with existing numerical literature, confirming the results' reliability.

Review History:

Received: Jun. 25, 2025

Revised: Sep. 20, 2025

Accepted: Oct. 05, 2025

Available Online: Oct. 07, 2025

Keywords:

Transient Flow

Natural Convection

Entropy Generation

Heat Transfer

Bifurcations

1- Introduction

Natural convection (NC) is induced by buoyancy forces arising from density gradients generated by temperature variations in a gravitational field. This phenomenon plays a crucial role in numerous engineering applications such as heat exchangers, building heating and ventilation systems, electronic component cooling, solar energy collectors, and thermal energy storage systems. Buoyancy-induced flows have been extensively studied across a wide range of cavity geometries and boundary conditions, employing both analytical and numerical approaches to examine the associated heat transfer (HT) and fluid flow behaviors.

Stratified fluids play a fundamental role in understanding and predicting phenomena in oceans, atmosphere, industrial systems, and various other domains. Their layered nature influences energy transfer, stability, mixing, and dynamics, making them vital in both scientific research and practical applications. Angirasa and Srinivasan [1] studied NC in thermally stratified, low-porosity porous media, reporting limited sensitivity of flow reversal to stratification. Chen and Eichhorn [2] explored NC from a uniform thermal plate in a stratified fluid kept in a cubical tank, emphasizing the influence of vertical thermal gradients. Tripathi and Nath

[3] numerically investigated NC in a thermally stratified fluid adjacent to a vertical uniform thermal wall. Their results showed a pronounced sensitivity of HT to both the wall temperature and the degree of ambient stratification, emphasizing the importance of buoyancy effects in layered environments. Rahaman et al. [4] conducted a comparative investigation of transient thermal convection in a stratified trapezoidal enclosure filled with air and water, with the upper boundary maintained at a uniformly low temperature. Their study emphasized the influence of fluid flow and HT mechanisms for the two different fluids. In a subsequent work, Rahaman et al. [5] analyzed the transition from laminar to turbulent regimes in a trapezoidal enclosure featuring a uniformly heated bottom wall, a cooled top boundary, and thermally insulated sloped sidewalls. Their findings revealed that, with increasing Ra, the system underwent a transition toward chaotic HT behavior, highlighting the sensitivity of NC to thermal boundary intensities and geometrical configurations.

Natural convection within enclosures plays a vital role in an extensive range of engineering and geophysical applications. The geometry of the enclosure, thermal boundary conditions, and fluid properties are critical parameters governing convective HT and flow dynamics. Numerous studies have examined NC in non-rectangular and inclined geometries to elucidate the complex interplay of these

*Corresponding author's email: mahfuz0809@gmail.com



Copyrights for this article are retained by the author(s) with publishing rights granted to Amirkabir University Press. The content of this article is subject to the terms and conditions of the Creative Commons Attribution 4.0 International (CC-BY-NC 4.0) License. For more information, please visit <https://www.creativecommons.org/licenses/by-nc/4.0/legalcode>.

factors. For instance, Bhowmick et al. [6] and Wang et al. [7] analyzed V-shaped cavities, revealing flow bifurcations and identifying critical HT characteristics. Similarly, Patterson and Imberger [8] showed that initial flow states in rectangular enclosures are highly sensitive to Ra and aspect ratio. Lee [9] extended this understanding through numerical studies on tilted cavities, demonstrating how variations in wall inclination and aspect ratio influence the Nusselt number and flow regimes. Investigations by Ma and Xu [10], Varol et al. [11], and Saha [12] further explored HT enhancement mechanisms, including fin placement, porous media, and transient heating. Additional studies by Bouafia and Daube [13], Xu et al. [14], and Iyican et al. [15] have revealed how localized heating and internal structures affect convective behavior. Rahman et al. [16] numerically examined MHD free convection over a vertical porous plate in a rotating system with an induced magnetic field, showing that magnetic and rotational effects suppress primary velocity while enhancing secondary velocity, and that stronger magnetic fields increase temperature, concentration, and associated transport rates. Natarajan [17] employed numerical methods to simulate NC in a trapezoidal cavity with non-uniform wall heating, capturing the complexity of flow induced by geometric and thermal asymmetry. Collectively, these studies highlight the intricate dependence of NC on enclosure configuration and boundary conditions, underscoring the need for continued investigation into such systems.

The square cavity serves as a fundamental model for studying NC due to its geometric simplicity and well-defined boundary conditions, rendering it ideal for both theoretical analysis and numerical validation. It offers a controlled setting for investigating complex heat and fluid flow phenomena, including boundary layer development, thermal stratification, flow instabilities, and transitions from laminar to turbulent regimes. Davis [18] initiated foundational work on two-dimensional NC with differentially heated vertical walls, while Basak et al. [19] extended the analysis to a cavity with a heated base and isothermal sidewalls, elucidating key flow structures under laminar conditions. Raji et al. [20] examined configurations involving inclined insulated walls and identified strong sensitivity of flow behavior to Ra and boundary orientation. Non-Boussinesq effects in low-Prandtl-number fluids were explored by Pesso and Piva [21], who emphasized the influence of density variation on heat transport mechanisms. Kouroudis et al. [22] explored the effect of constant heat fluxes on thermal stratification in the cavity, revealing intricate circulation patterns. Further complexity was introduced by Deng [23], who analyzed the effects of source-sink distributions along cavity walls, highlighting the role of spatial thermal forcing on flow structure. Barakos et al. [24] conducted high-fidelity simulations over a wide range of Ra, validating numerical accuracy and capturing the transition from laminar to turbulent regimes. Collectively, these studies reinforce the square cavity's role as a benchmark configuration for advancing understanding of NC dynamics under controlled conditions. Recently, Bawazeer and Alsoofi [25] examined the effect of Ra and Pr on HT and flow patterns

within a square cavity featuring adiabatic horizontal walls and vertically oriented heated and cooled walls.

Entropy generation analysis has emerged as a vital framework for assessing the thermodynamic efficiency of convective HT systems. Rooted in the second law of thermodynamics, this approach enables the quantification of irreversibilities arising from thermal gradients and viscous dissipation, thereby offering a pathway for system optimization. Bejan [26] pioneered this methodology by establishing a theoretical foundation for entropy-based performance evaluation in HT processes, emphasizing constraints related to size, time, and efficiency. Subsequent studies have extended this framework to complex geometries and flow conditions. Biswal and Basak [27] analyzed E_{gen} in curved-walled enclosures, identifying peak thermal irreversibility near concave wall mid-heights, with minor contributions from fluid friction. Bouabid et al. [28] demonstrated that increasing aspect ratios in inclined rectangular cavities at high Grashof numbers amplify total E_{gen} . Oliveski et al. [29] reported strong thermal-hydrodynamic coupling in vertically stratified rectangular enclosures, where heat and flow fields jointly influence irreversibility. In trapezoidal configurations, Rahaman et al. [30, 31] showed that higher Ra values elevate entropy production and degrade energy efficiency. Studies by Singh [32] and Ilis et al. [33] further underscored the roles of wall orientation and aspect ratio in modulating irreversibility distribution. Sheremet et al. [34] introduced nanofluids and particle effects, such as Brownian motion and thermophoresis, revealing increased entropy generation with higher thermal gradients. Sabo [35] explored entropy mechanisms in octagonal cavities with embedded cold elements, while Shavik [36] found that cavity inclination predominantly affects fluid friction irreversibility.

Although NC within square cavities has been extensively investigated, limited attention has been devoted to the combined effect of a uniformly heated bottom wall, a cooled top wall, and linearly stratified vertical walls, particularly in the context of transient bifurcations and E_{gen} . Thermal stratification along the vertical walls of a square cavity arises from temperature gradients induced by differential heating, resulting in stratified fluid motion and buoyancy-driven convection. This phenomenon has important practical applications in engineering and environmental systems, including building and room ventilation, solar energy storage systems, and environmental and atmospheric studies. To the best of the authors' knowledge, the present study is among the first to provide a comprehensive investigation of the sequence of pitchfork and Hopf bifurcations, the transition to chaos, and the evolution of E_{gen} under this configuration. The primary objective is to explore the effect of the Ra on flow dynamics and thermodynamic irreversibility, with particular emphasis on identifying critical Ra values that signify transitions such as pitchfork bifurcation, Hopf bifurcation, and the onset of chaotic behavior. A comprehensive analysis of HT and E_{gen} is performed to assess its variation across different flow regimes and its implications for enhancing the thermodynamic performance of convective systems. To

confirm the reliability of the findings, the present numerical outcomes are validated through comparison with a previously published study.

2- Methodology

This research is mainly intended to investigate the unsteady NC heat transfer, E_{gen} within a square cavity applying a two-dimensional numerical simulation approach. For laminar flow, a two-dimensional approach is sufficient to capture the essential fluid flow characteristics, as three-dimensional effects do not lead to significant variations in this configuration. Fig. 1 illustrates the schematic of the physical domain along with the corresponding boundary conditions. The bottom wall of the cavity is maintained at a uniform high temperature, represented as T_h , which is higher compared to the temperature of the top wall, labeled T_c . The vertical sidewalls exhibit a linear thermal stratification, denoted by T_i . The fluid in the cavity specified by a Pr of 7.01 for initially stratified water. The thermo physical properties of stratified air are presented in Table 1. All enclosure boundaries are assumed to be stationary and subject to no-slip conditions.

In a square enclosure, the NC flow of stratified water is investigated using a 2D model governed by the coupled Navier-Stokes and energy equations, formulated under the Boussinesq approximation. The dimensional governing equations describe the evaluation of NC flow in the cavity as (refer to Rahaman et al. [37]):

$$\frac{\partial U}{\partial X} + \frac{\partial V}{\partial Y} = 0, \quad (1)$$

$$\frac{\partial U}{\partial t} + U \frac{\partial U}{\partial X} + V \frac{\partial U}{\partial Y} = -\frac{1}{\rho} \frac{\partial P}{\partial X} + \nu \left(\frac{\partial^2 U}{\partial X^2} + \frac{\partial^2 U}{\partial Y^2} \right), \quad (2)$$

$$\frac{\partial V}{\partial t} + U \frac{\partial V}{\partial X} + V \frac{\partial V}{\partial Y} = -\frac{1}{\rho} \frac{\partial P}{\partial Y} + \nu \left(\frac{\partial^2 V}{\partial X^2} + \frac{\partial^2 V}{\partial Y^2} \right) + g \beta (T - T_0), \quad (3)$$

$$\frac{\partial T}{\partial t} + U \frac{\partial T}{\partial X} + V \frac{\partial T}{\partial Y} = \alpha \left(\frac{\partial^2 T}{\partial X^2} + \frac{\partial^2 T}{\partial Y^2} \right). \quad (4)$$

Dimensional boundary condition are as follows:

$$\begin{cases} \text{Top cold wall: } T = T_c, U = V = 0, \\ \text{Bottom heated wall: } T = T_h, U = V = 0, \\ \text{Vertical stratified walls: } T = T_i, U = V = 0. \end{cases} \quad (5)$$

The following are the normalized variables that were utilized:

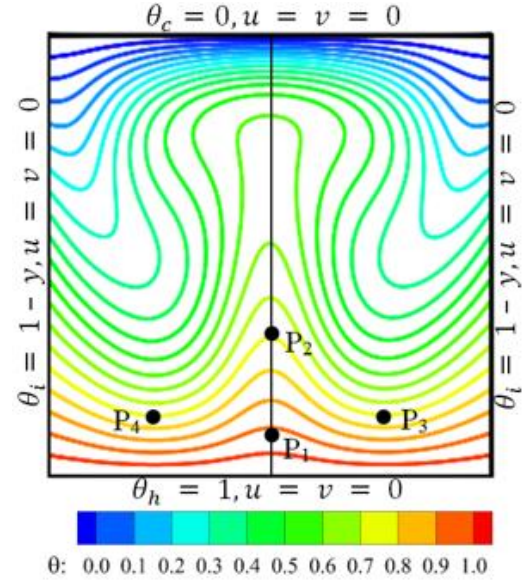


Fig. 1. Physical domain and normalized boundary conditions, indicating key points $P_1(0, 0.2)$, $P_2(0, 0.5)$, $P_3(0.6, 0.3)$, and $P_4(-0.6, 0.3)$ utilized in the resulting figures.

$$\begin{aligned} x &= \frac{X}{Y}, y = \frac{Y}{H}, u = \frac{UH}{\alpha\sqrt{\text{Ra}}}, v = \frac{VH}{\alpha\sqrt{\text{Ra}}}, \\ p &= \frac{PH^2}{\rho\alpha^2\text{Ra}}, \theta = \frac{T - T_\infty}{T_h - T_c}, \tau = \frac{t\alpha\sqrt{\text{Ra}}}{H^2}. \end{aligned} \quad (6)$$

Two results controlling parameters; Prandtl number (Pr) and Rayleigh number (Ra) (refer to Rahaman et al. [38]) as:

$$\text{Pr} = \frac{\nu}{\alpha} \text{ and } \text{Ra} = \frac{g\beta(T_h - T_c)H^3}{\nu\alpha}. \quad (7)$$

The normalized form of Eqs. (1) to (4) becomes (refer to Rahaman et al. [38]):

$$\frac{\partial u}{\partial x} + \frac{\partial v}{\partial y} = 0, \quad (8)$$

$$\frac{\partial u}{\partial \tau} + u \frac{\partial u}{\partial x} + v \frac{\partial u}{\partial y} = -\frac{\partial p}{\partial x} + \frac{\text{Pr}}{\sqrt{\text{Ra}}} \left(\frac{\partial^2 u}{\partial x^2} + \frac{\partial^2 u}{\partial y^2} \right), \quad (9)$$

$$\frac{\partial v}{\partial \tau} + u \frac{\partial v}{\partial x} + v \frac{\partial v}{\partial y} = -\frac{\partial p}{\partial y} + \frac{\text{Pr}}{\sqrt{\text{Ra}}} \left(\frac{\partial^2 v}{\partial x^2} + \frac{\partial^2 v}{\partial y^2} \right) + \text{Pr} \theta, \quad (10)$$

$$\frac{\partial \theta}{\partial \tau} + u \frac{\partial \theta}{\partial x} + v \frac{\partial \theta}{\partial y} = \frac{1}{\sqrt{\text{Ra}}} \left(\frac{\partial^2 \theta}{\partial x^2} + \frac{\partial^2 \theta}{\partial y^2} \right). \quad (11)$$

where, u , v , x , y , p , τ and θ denote the normalized forms of U , V , X , Y , P , t and T , respectively.

The following are the boundary conditions in normalized form:

$$\begin{cases} \theta_c = u = v = 0, \text{ at the top wall} \\ \theta_h = 1, u = v = 0, \text{ at the bottom wall} \\ \theta_i = 1 - y, u = v = 0, \text{ at the vertical walls.} \end{cases} \quad (12)$$

The following equation defines the average Nusselt number on the horizontal walls, denoted as Nu_h and on the vertical walls, denoted as Nu_v (refer to Rahaman et al. [38, 39]):

$$Nu_h = \frac{1}{l} \int_0^l \frac{\partial \theta}{\partial y} dx \text{ and } Nu_v = \frac{1}{l} \int_0^1 \frac{\partial \theta}{\partial x} dy. \quad (13)$$

In a NC system, thermodynamics irreversibility arises primarily from two mechanisms: HT and fluid friction (FF). Based on linear transport theory, the normalized local E_{gen} corresponding to these processes can be expressed as follows (refer to [30, 31] for more details):

$$E_{ht} = \left(\frac{\partial \theta}{\partial x} \right)^2 + \left(\frac{\partial \theta}{\partial y} \right)^2. \quad (14)$$

$$E_{ff} = \psi \left[2 \left\{ \left(\frac{\partial u}{\partial x} \right)^2 + \left(\frac{\partial v}{\partial y} \right)^2 \right\} + \left(\frac{\partial u}{\partial y} + \frac{\partial v}{\partial x} \right)^2 \right]. \quad (15)$$

where E_{ht} and E_{ff} denote the local E_{gen} resulting from the HT and FF. In Eq. (15), ψ is referred to as the irreversibility distribution ratio, which is defined as:

$$\psi = \frac{\mu T_\infty}{\alpha} \left(\frac{k}{L \Delta T} \right)^2. \quad (16)$$

The local E_{gen} in the cavity, represented as E_l , define as the sum of E_{ht} and E_{ff} (refer to Rahaman et al. [30]):

$$E_l = E_{ht} + E_{ff}. \quad (17)$$

The local Bejan number Be_l is defined as follows (see Rahaman et al. [30]):

$$Be_l = \frac{E_{ht}}{E_{ht} + E_{ff}}. \quad (18)$$

2- 1- Numerical Model

In this study, the finite volume (FV) method based ANSYS Fluent 17.0 software was employed to solve the governing Eqs. (8) to (11), along with the boundary conditions specified in Eq. (12) (refer to Rahaman et al. [30, 31], for details). To interaction of the pressure-velocity coupling, the SIMPLE (Semi-Implicit Method for Pressure-Linked Equations) method is employed. The viscous components are approximated through a second-order central differencing method, whereas a third-order QUICK (Quadratic Upstream Interpolation for Convective Kinematics) scheme is utilized for the advection terms. A non-uniform rectangular mesh structure is utilized to improve spatial accuracy in the numerical domain. Under-relaxation factors are also used to solve the discretized governing equations to maintain the stability of the iterative process, as described in the reference (refer to Rahaman et al. [37, 38]). The unstable terms in temporal discretization are addressed using a second-order accurate implicit time integration technique, consistent with the approaches outlined by Patterson and Imberger [8]. The convergence requirements are rigorously established, with residuals for continuity, momentum, and energy equations fixed at 10^{-5} to guarantee solution precision.

Table 1. Thermo physical properties of fluid (refer to Rahaman et al. [30]).

Property (unit)	Stratified fluid (water)
Density, ρ (kg/m ³)	1.177
Specific heat, C_p (J/kg K)	1012
Viscosity, μ (kg/m s)	0.000018
Thermal conductivity, k (W/m K)	0.00257887

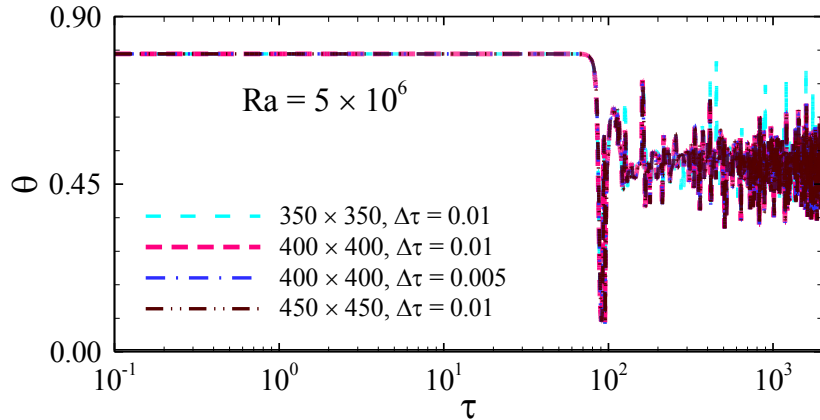


Fig. 2. Temperature time series at P1 (0, 0.2) for $\text{Ra} = 5 \times 10^6$ with different grids and time steps.

Table 1. Temperature at $P_1 (0, 0.2)$ using different grids and time steps.

Grids and time steps	Average temperature	Variance
350×350 and $\Delta\tau = 0.01$	0.5142	0.87%
400×400 and $\Delta\tau = 0.01$	0.5187	-
400×400 and $\Delta\tau = 0.005$	0.5198	0.21%
450×450 and $\Delta\tau = 0.01$	0.5202	0.29%

2- 2- Grid and Time Step Dependent Tests

The grid resolution used in the computational domain plays a crucial role in determining the stability and accuracy of numerical results. To measure the sensitivity to grid size and time step, a comparative analysis was performed for the maximum Ra, under the hypothesis that the grid and time step optimized for this extreme Ra would also be adequate for scenarios with smaller Ra values. For this purpose, three symmetric grid configurations (350×350 , 400×400 , and 450×450) and two distinct time steps (0.01 and 0.005) were selected for evaluation. Fig. 2 presents the TTS at point $P_1 (0, 0.2)$ obtained using different grids and time steps for $\text{Ra} = 5 \times 10^6$. The recorded temperatures, derived from the various grids and time steps, show consistency during the initial period and slight divergence in the later stages.

Table 2 illustrates the variation in average temperature at the fully developed (FDS) flow regime for various grids size and time steps to assess grid independence test. A significant disparity of around 0.87% was seen between the simulations utilizing the coarsest grid 350×350 and the finest grid 400×400 . The disparity in average temperature between the two finer meshes 400×400 and 450×450 was modest, approximately 0.29%. Following this analysis, a mesh resolution of 400×400 and a time increment of 0.001 were

chosen to ensure computational accuracy and efficiency for all subsequent simulations.

In this research, the normalized dissipative time scale computed using the following equation (refer to Rahaman et al. [31] for details):

$$\lambda_k = \left(32\pi\sqrt{2}\right)^{1/4} \left(\frac{\text{Ra}}{\text{Pr}}\right)^{-3/8}. \quad (19)$$

Here, $\lambda_k = 0.02204$ for $\text{Ra} = 5 \times 10^6$; so, the normalized time steps of 0.005 and 0.01 are selected for the comparison.

2- 3- Model Validation

Model validation is a critical component of any numerical investigation to confirm the accuracy and credibility of the results. In this research, the comparison was done explicitly against the numerical data presented by Basak et al. [19], who utilized the finite element method to examine laminar NC heat transport in a square cavity. In their study, the lower boundary of the cavity was uniformly heated, while vertical walls were maintained at a uniform low temperature. The upper wall, conversely, was thermally insulated. To ensure consistency, the comparison was conducted using non-

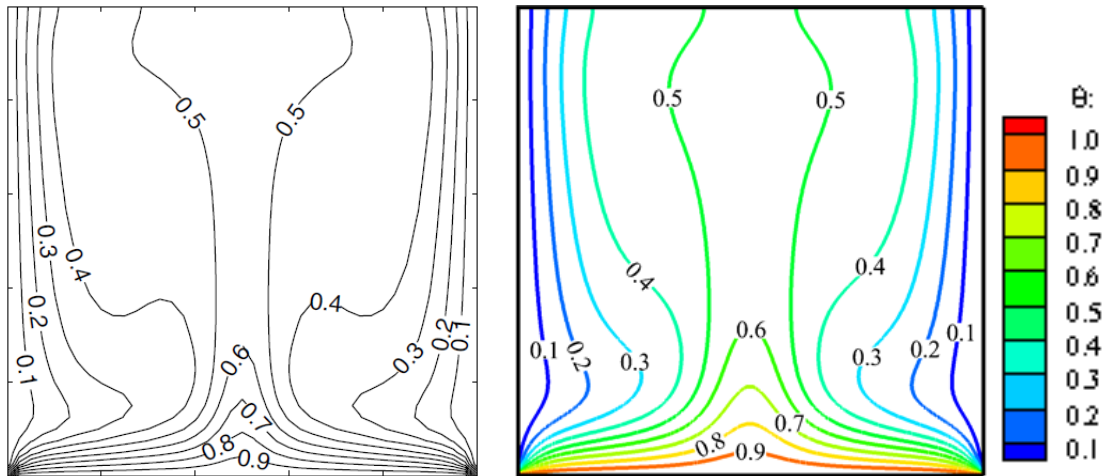


Fig. 3. Comparison of present results with Basak et al. [19] for a square cavity when $Pr = 10$ and $Ra = 10^5$.

dimensional characteristics, specifically a Ra of 10^5 and a Prandtl number of 10. Fig. 3 illustrates that the temperature contour patterns derived from the current finite volume-based simulation closely align with those of Basak et al. [19], hence confirming the accuracy and dependability of the established computational model.

3- Results and Discussions

The numerical approach employed in this study has been validated and subsequently utilized to investigate NC, HT, and E_{gen} within a thermally stratified square enclosure. The cavity configuration consists of a uniformly heated bottom wall, a cooled top wall, and thermally stratified vertical sidewalls. A comprehensive series of two-dimensional simulations has been conducted across a broad range of Ra , spanning from 10^0 to 5×10^6 , with a fixed Pr of 7.01. As the Ra increases, the system undergoes a sequence of bifurcations. These bifurcations mark the evolution of the flow field from a symmetric, conduction-dominated regime at lower Ra values to increasingly complex and chaotic convective patterns at higher Ra values. The resulting flow structures and associated thermal behaviors are analyzed in detail in the following sections.

3- 1- Symmetric Flow

Initially, the bottom surface of the cavity is uniformly heated, while the vertical sidewalls exhibit thermal stratification, and the top wall is kept at a constant cooled temperature. These thermal boundary conditions lead to the formation of thermal boundary layers along the interior surfaces of the cavity. The resulting temperature gradients, coupled with gravitational effects, give rise to buoyancy-driven flow circulation within the enclosure. Fig. 4 illustrates isotherm and streamlines plots for Ra ranging from 10^0 to 10^3 . At these relatively low Ra values, the flow remains predominantly conduction-driven, as observed in Fig. 4(a) to Fig. 4(d). The streamlines plots reveal that the thermal

field within the cavity is largely aligned along the vertical (y) axis, indicating the absence of significant convective activity. Furthermore, no distinct rising or falling plumes are evident within these Ra values, confirming that conduction is the dominant mode of HT under these conditions.

3- 2- Asymmetric Flow

In Fig. (4) Shows that, for Ra in the range of 10^0 and 10^3 , the fluid flow exhibits symmetrical behavior within the enclosure with respect to the y -axis. To examine the onset of asymmetry, detailed analyses of the streamline and isotherm plots were conducted at $Ra = 8 \times 10^3$ and 10^4 . At $Ra = 8 \times 10^3$ the flow remains symmetric steady, as illustrated in Fig. 5(a) and Fig. 5(c). However, at $Ra = 10^4$ the flow becomes increasingly dynamic, characterized by the formation of two dominant convective cells that begin to migrate laterally toward the center of the cavity, as depicted in Fig. 5(b) and Fig. 5(d). The symmetry observed at lower Ra gradually breaks down, indicating the system's departure from its previously stable configuration.

This transition signifies the onset of a pitchfork bifurcation, wherein the initially symmetric flow evolves into an asymmetric state. The development of this asymmetry indicates the emergence of Rayleigh-Bénard-type instability, marking a critical transition in the flow regime from stable, symmetric convection pattern to a more complex and asymmetric behavior. This transition reflects a fundamental change in the flow dynamics, governed by increasing thermal driving forces.

To analyze the onset of pitchfork bifurcation in more detail, a bifurcation diagram is constructed in the $Ra-u$ plane, as shown in Fig. 6. The bifurcation diagram (refer to [39], for details) indicates that for $Ra = 8 \times 10^3$, the x -velocity u at the point $P_1(0, 0.2)$ remains approximately zero. This behavior indicates that the flow retains its symmetry with respect to the cavity's vertical centerline at this Ra . However, as the Ra increases to $Ra = 10^4$, a symmetry-breaking bifurcation

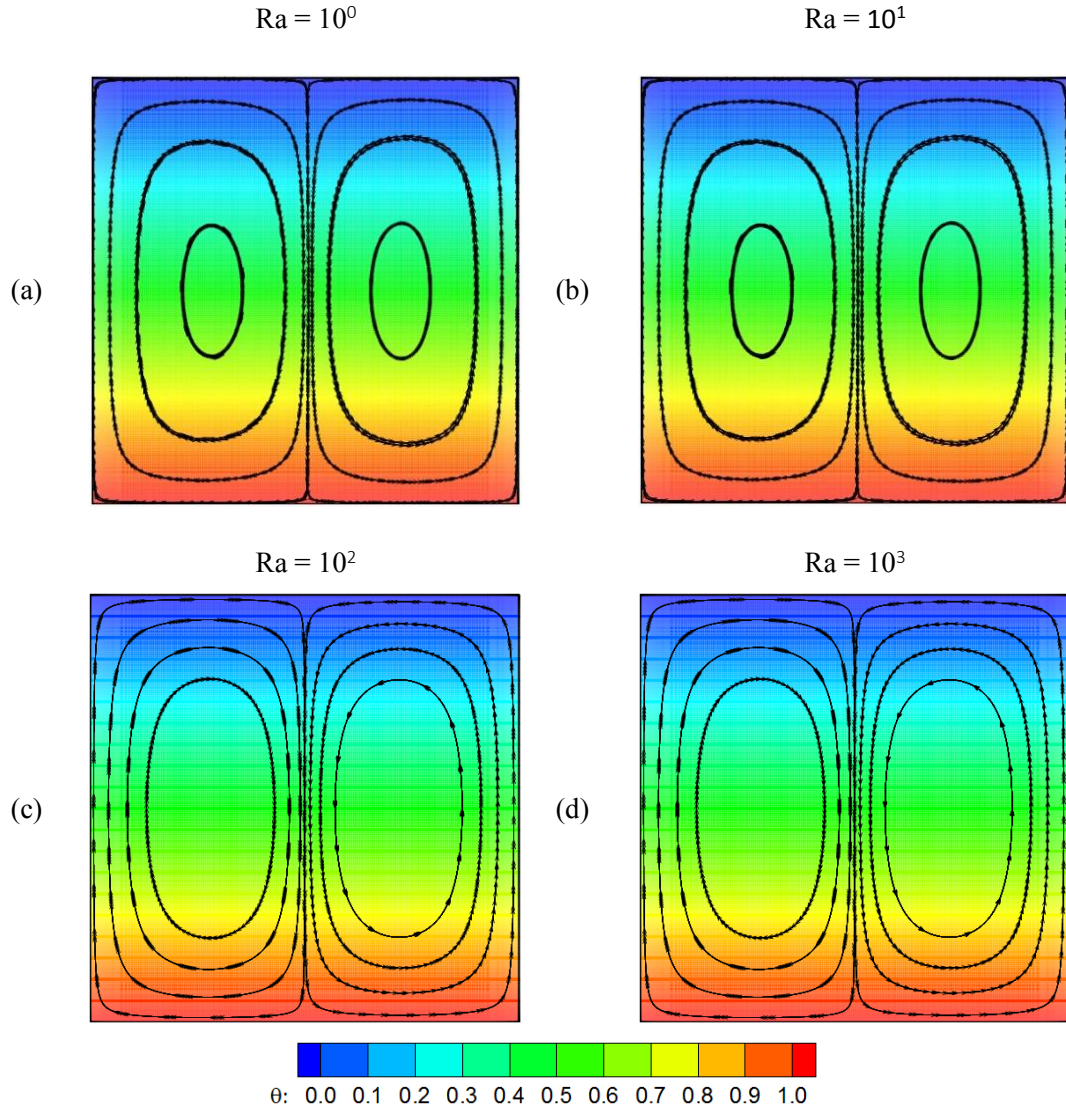


Fig. 4. Isotherm and streamline plots for smaller Ra values at the FDS.

becomes evident: the x -velocity at P_1 deviates from zero, signaling the onset of an asymmetric flow structure. This deviation manifests in two distinct solution branches: in one branch, marked by blue circular symbols, the x -velocity increases in the positive direction, while in the other branch, denoted by purple square markers, it decreases in the negative direction. The appearance of these two divergent solution paths is a hallmark of a supercritical pitchfork bifurcation. This transition signifies a critical change in the system's dynamics, where the steady, symmetric solution loses stability and shifts to asymmetric state.

3- 3- Unsteady Flow

Figure 7 displays the TTS and associated spectral study at point $P_3(0.6, 0.3)$ for increased Ra, demonstrating the change from steady to chaotic flow. At $\text{Ra} = 2 \times 10^5$, the flow remains constant throughout the FDS, as illustrated in Fig. 7(a). As Ra

raises to 3×10^5 , the flow transitions into a periodic regime, as described in Fig. 7(b), indicating the presence of a Hopf bifurcation among these two Ra values. The spectral plots in Fig. 7(c) and Fig. 7(e) further substantiate the analysis by illustrating the dominant harmonic frequencies $f_p = 0.0129$ and 0.0432 associated with the periodic behavior at $\text{Ra} = 3 \times 10^5$ and $\text{Ra} = 10^6$, respectively.

With an increase in the Ra, significant alterations in flow behavior are observed, especially the transition from periodic to chaotic motion. At $\text{Ra} = 10^6$, the flow demonstrates periodic behavior; however, at $\text{Ra} = 2 \times 10^6$, it shifts to a chaotic regime, signifying a secondary bifurcation between these values. Spectral analysis at $\text{Ra} = 2 \times 10^6$ (Fig. 7(g)) indicates destabilization of the principal frequency and the lack of sub harmonic peaks, thereby providing clear evidence for the transition to chaos.

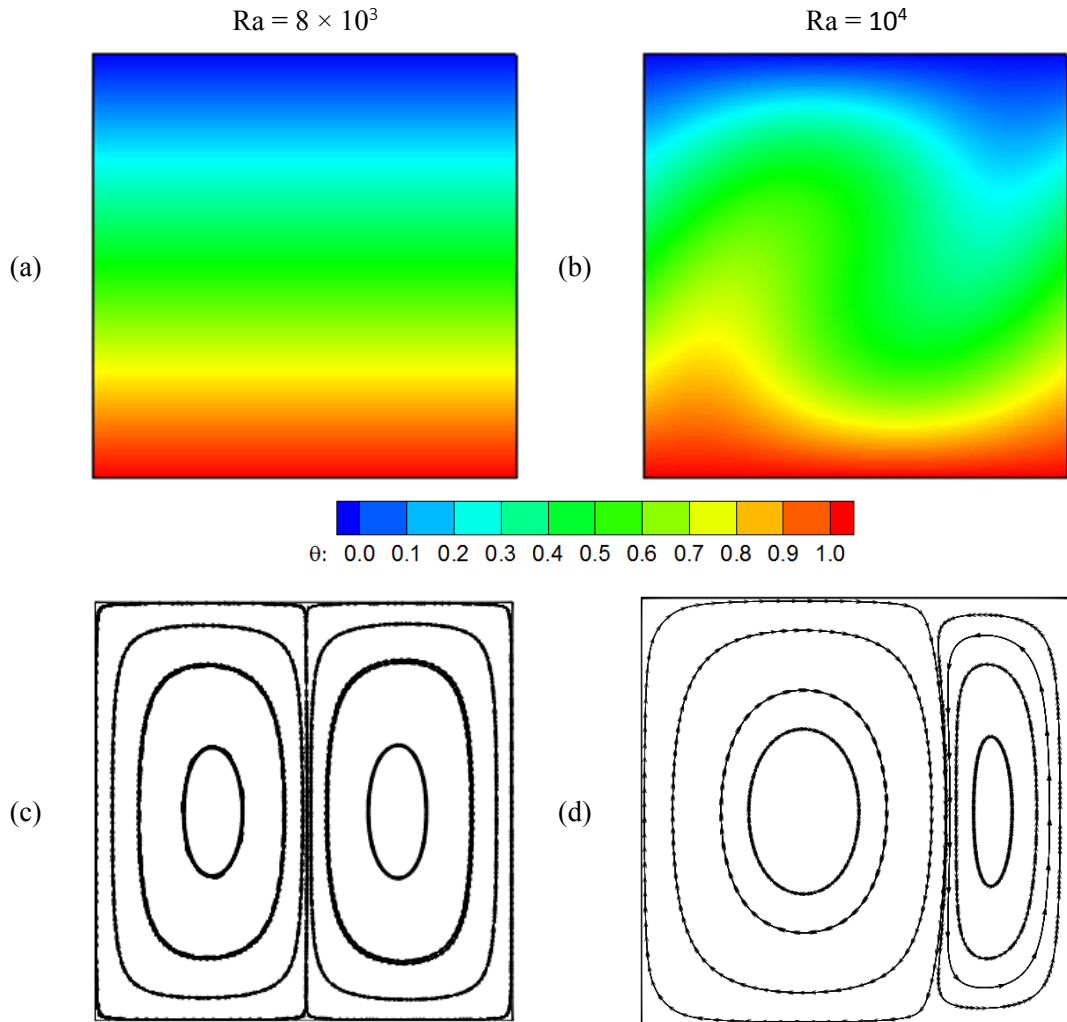


Fig. 5. Visualization of the pitchfork bifurcation through isotherm and streamline contour. Subfigures (a, c) and (b, d) show the symmetric and asymmetric flow regimes, respectively, for different Ra.

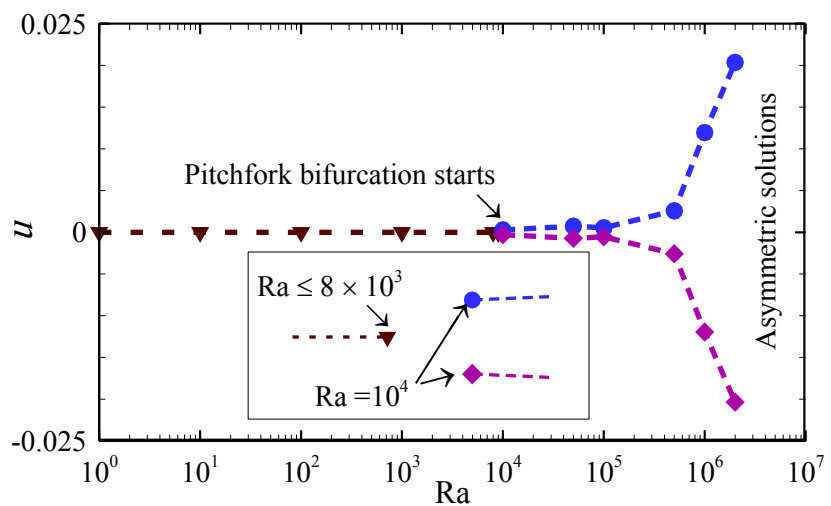


Fig. 6. Pitchfork bifurcation diagram in the $\text{Ra}-u$ plane, where u denotes the x-velocity at point $P_1(0, 0.2)$.

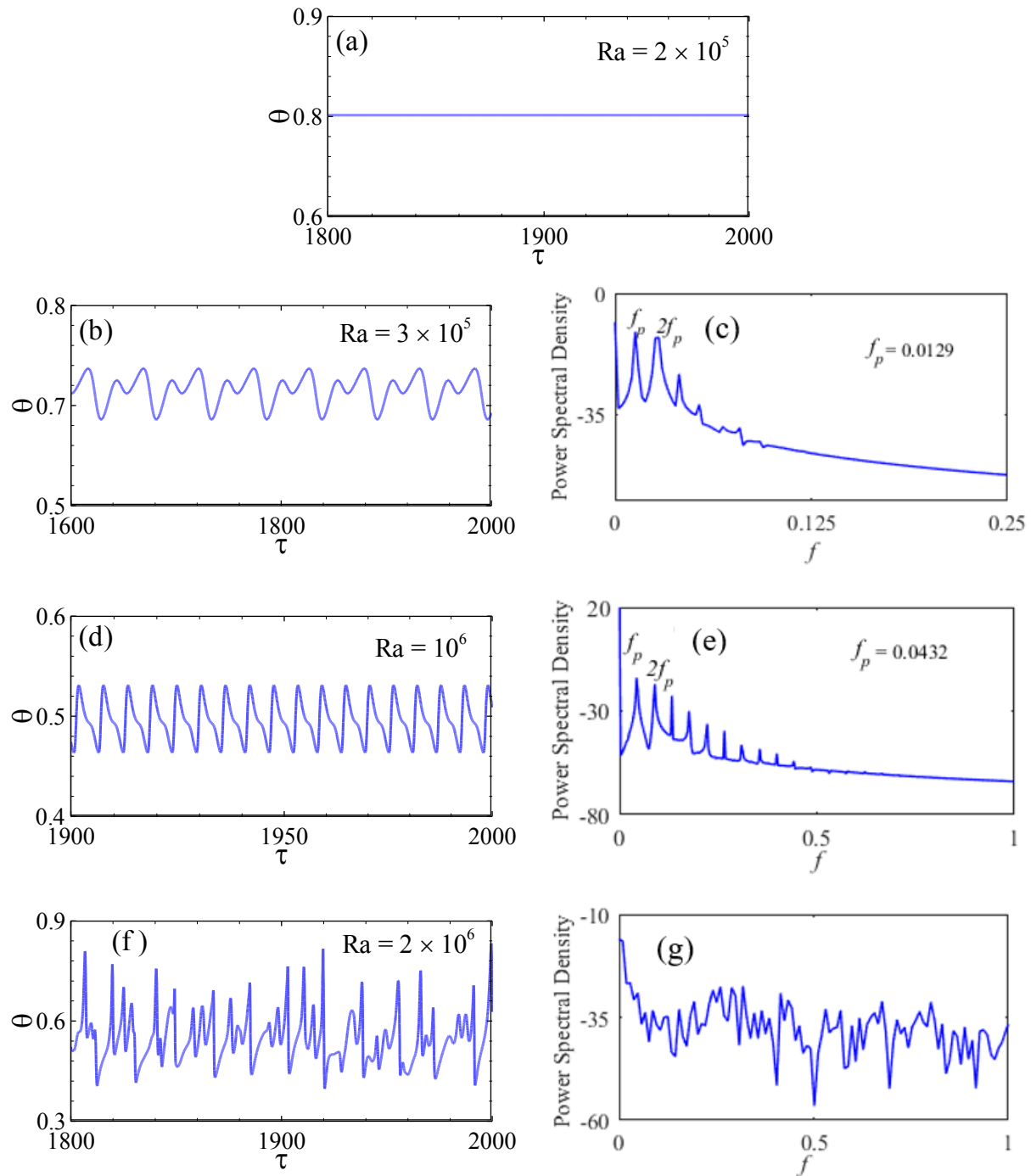


Fig. 7. Temperature time series and the corresponding spectral analysis at point P_3 (0.6, 0.3): (a) steady state for $\text{Ra} = 2 \times 10^5$; (b, c) shifting to periodic state for $\text{Ra} = 3 \times 10^5$; (d, e) remains periodic for $\text{Ra} = 10^6$; and (f, g) changeover to chaotic state for $\text{Ra} = 2 \times 10^6$.

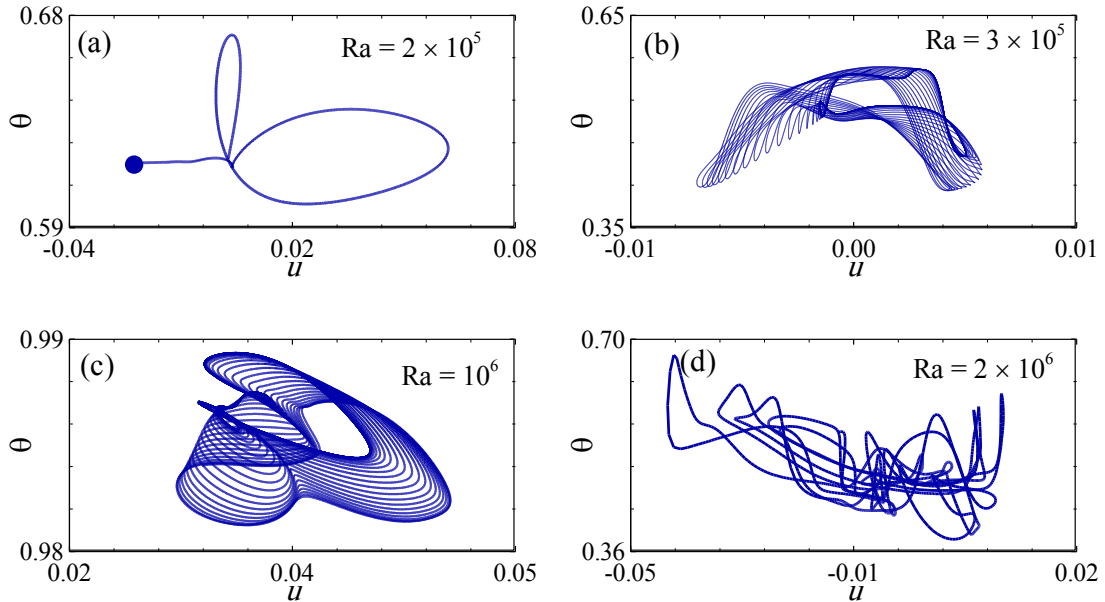


Fig. 8. Limit point and limit cycle P_4 (-0.6, 0.3): (a) for $Ra = 2 \times 10^5$, (b) for $Ra = 3 \times 10^5$, (c) for $Ra = 10^6$, and (d) for $Ra = 2 \times 10^6$.

The v - θ phase portraits at point P_4 (-0.6, 0.3) are analyzed over the range of $\tau = 1000$ to 2000 to enhance the understanding into the unsteady dynamics. At $Ra = 2 \times 10^5$ (Fig. 8(a)), the system reaches a stable fixed point. A closed-loop trajectory emerges at $Ra = 3 \times 10^5$ (Fig. 8(b)), indicating a stable limit cycle and signaling the onset of Hopf bifurcation (refer to [40], for more details). Fig. 8(c) illustrates that periodic limit cycles are maintained at $Ra = 10^6$. At $Ra = 2 \times 10^6$, Fig. 8(d), demonstrates erratic, non-repeating trajectories, indicating that the system has transitioned into a chaotic regime. This progression highlights the significant role of bifurcations in regulating transitions in NC behavior at higher Ra .

4- Entropy Generation

This section presents a detailed analysis of entropy generation (E_{gen}) due to both thermal gradients (E_{th}) and viscous dissipation (E_{ff}) along with the evaluation of local E_{gen} (E_l) and the local Bejan number (Be_l), as illustrated in Fig. 9. At $Ra = 10^0$ to 10^5 , the effects of buoyancy forces are minimal, resulting in nearly uniform flow structures. Consequently, HT is dominated by conduction, and E_{gen} is primarily governed by thermal gradients. Due to the limited variation in entropy fields and the dominance of conductive HT, E_{gen} plots for these lower Ra values are omitted.

As the Ra increases, buoyancy-driven convection becomes more pronounced. This intensifies fluid motion, enhancing the contribution of fluid friction (FF) to the local E_{gen} . At Ra of 2×10^5 , HT predominantly influences E_{gen} , whereas FF impact is negligible. The following Fig. 9 also demonstrate that an increase in Ra leads to a decrease in E_{gen} attributed to HT while simultaneously causing an increase in E_{gen} due to FF in the cavity. This transition suggests that at

$Ra = 10^6$, the influence of viscous dissipation is increasingly significant. The increase in buoyancy-driven flow at higher Ra values enhances fluid motion, consequently amplifying irreversibilities associated with fluid flow. In contrast, the diminished buoyant forces at lower Ra restrict fluid circulation, resulting in HT predominating in entropy production.

5- Heat Transfer

Although isotherms and streamlines are not direct measures of HT rates along enclosure surfaces, they provide significant qualitative insights into internal flow behavior and its influencing factors. Fig. 10 shows the time series of the average Nusselt number (Nu_h) at the bottom and top walls, and Nu_v at the left and right walls, reflecting the transient thermal response. The fluid within the cavity demonstrates thermal stratification, indicating that the temperature of the liquid adjacent to each boundary closely aligns with the wall temperatures, including those at the heated base, cooled top, and stratified vertical walls.

For the initial stratification reduces thermal gradients at the boundaries leading to minimal HT. As the system progresses from its initial state, stratification progressively diminishes, and convective activity prevails. In this transitional regime, fluctuations in the average Nusselt number (Nu) become apparent and intensify as the Ra increases, demonstrating enhanced convective effects. In the fully developed flow regime, the behavior of the Nu is contingent upon the Ra : it remains constant for $Ra \leq 2 \times 10^5$, transitions to periodic behavior at $Ra = 3 \times 10^5$, and displays chaotic oscillations for $Ra \geq 2 \times 10^6$. The observed behaviors correspond closely with the bifurcation and flow dynamics depicted in Fig. 7 and Fig. 8.

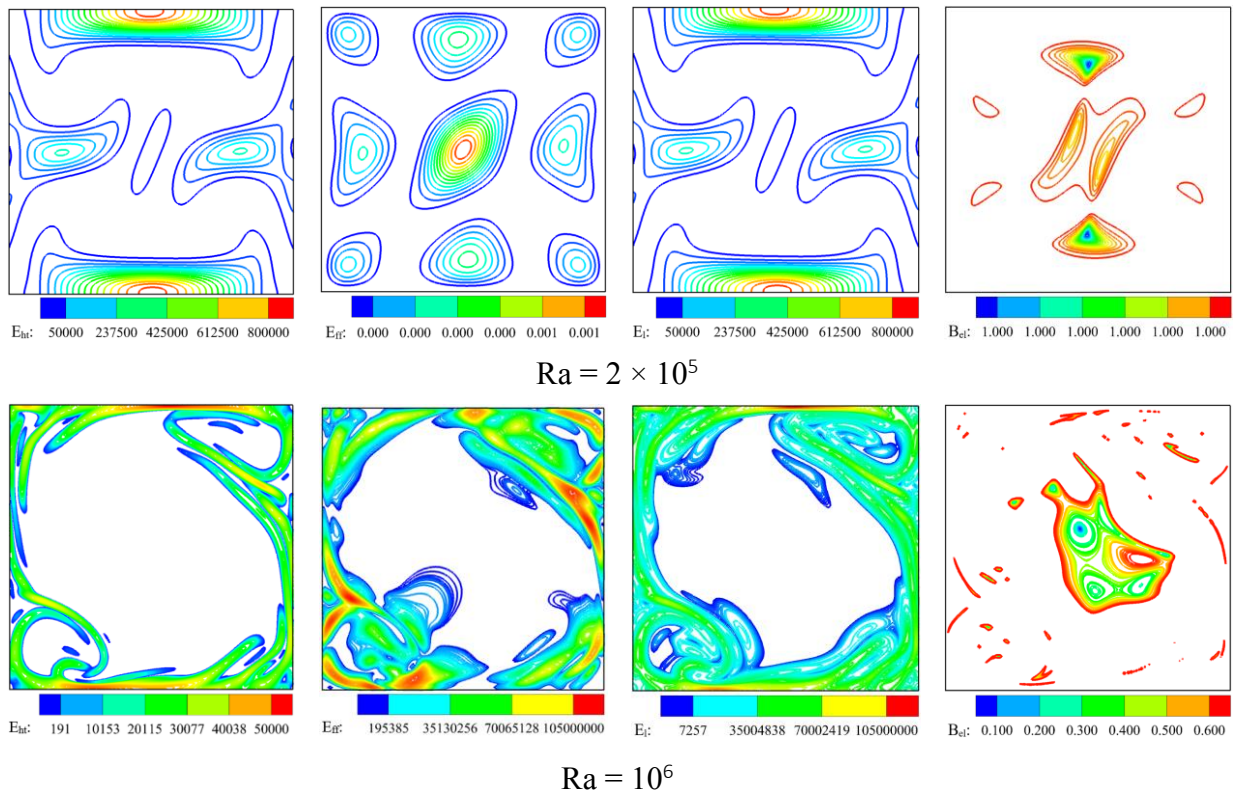


Fig. 9. Distribution of E_{gen} due to HT (E_{ht}), E_{gen} due to FF (E_{ff}), local E_{gen} (E_l), and local Bel for the Ra values of 2×10^5 and 10^6 , respectively.

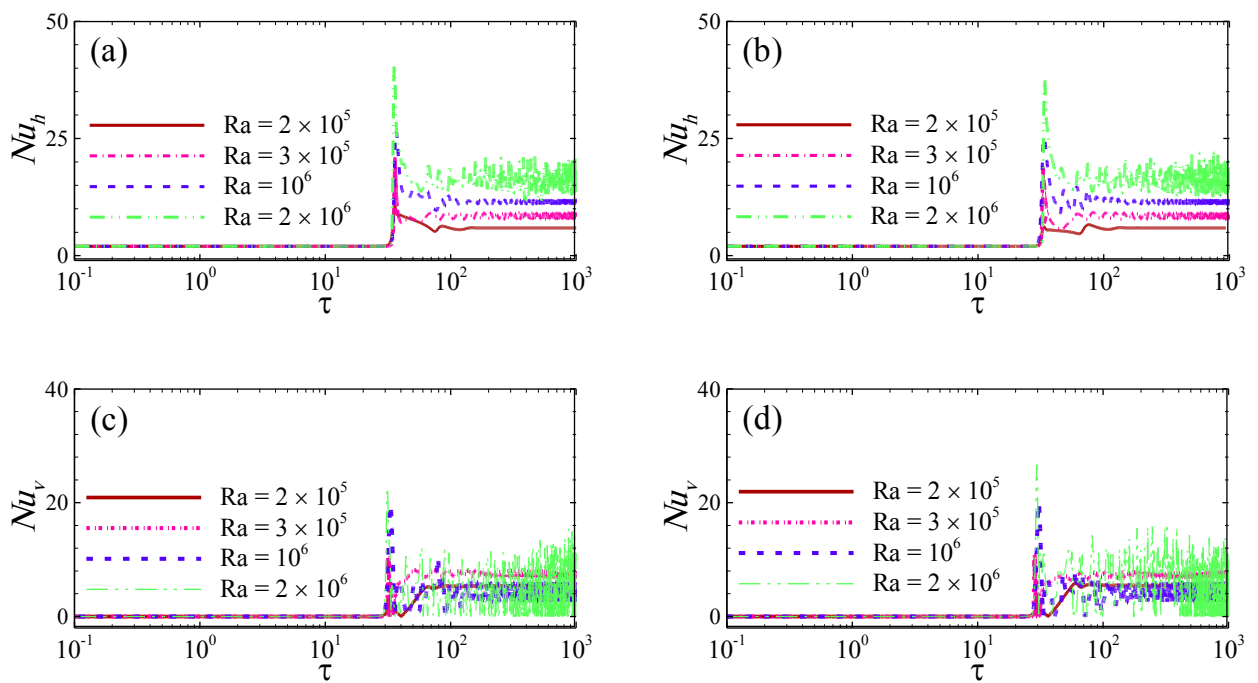


Fig. 10. Average Nusselt number time series for different Ra: (a, b) at the horizontal (bottom and top) walls; (c, d) at the vertical (left and right) walls.

6- Conclusions

This study examined NC, HT, and E_{gen} in a thermally stratified trapezoidal cavity encompassing stratified water. The FV method was employed for numerical simulations across a range of Ra from 10^0 to 5×10^6 , maintaining a Pr of 7.01.

Key findings are summarized as follows:

- Thermal boundary layers initially develop along the cavity walls, followed by the formation of the primary circulatory flow. During the transition phase, thermal plumes exhibit alternating rising and sinking behavior, leading to the establishment of well-defined cellular structures within the flow.
- For $\text{Ra} \leq 8 \times 10^3$, the flow is primarily dominated by conduction, and exhibits symmetry about the cavity's mid-plane.
- As the Ra increases, the flow undergoes a series of bifurcations that lead to qualitative changes in the flow regime. A pitchfork bifurcation occurs within the range of $\text{Ra} = 8 \times 10^3$ to 10^4 , resulting in symmetry breaking and the emergence of asymmetric flow behavior.
- A Hopf bifurcation occurs between $\text{Ra} = 2 \times 10^5$ and 3×10^5 , indicating the changeover from a steady asymmetric framework to a periodic flow.
- A further bifurcation occurs between $\text{Ra} = 10^6$ and 2×10^6 , leading to chaotic flow dynamics.
- The HT rate at the bottom and top walls is higher than that at the vertical walls, primarily due to the thermal stratification along the vertical walls.
- The analysis of entropy generation reveals that with increasing Ra, viscous dissipation becomes increasingly significant relative to thermal irreversibility. As a result, the overall entropy generation rises, suggesting a decline in the thermodynamic efficiency and an increase in energy degradation and potential environmental impact.

Nomenclature

Be_l	local Bejan number
Cp	specific heat (J/kg.K)
E_{ff}	entropy generation due to fluid friction
E_{gen}	entropy generation
E_{ht}	entropy generation due to heat transfer
E_l	local entropy generation
g	gravitational force (m/s ²)
H	length and height of the cavity (m)
k	thermal conductivity (W/(m·K))
P	pressure (N/m ²)
p	dimensionless pressure
Pr	Prandtl number

Ra Rayleigh number, $g\beta(T_h - T_c)H^3/\nu k$

t time (s)

T temperature (K)

T_c temperature of the top wall (K)

T_h temperature of the bottom wall (K)

T_i temperature of the inclined walls (K)

T_∞ environmental temperature (K)

U, V velocity components (m/s)

u, v dimensionless velocity components

X, Y coordinates

x, y dimensionless coordinates

Greek symbols

α thermal diffusivity (m²/s)

θ dimensionless temperature

ν kinematic viscosity (m²/s)

φ irreversibility distribution ratio

ψ inclination angle

ρ density (kg/m³)

τ dimensionless time

$\Delta\tau$ dimensionless time step

θ_c dimensionless temperature of the top wall

θ_h dimensionless temperature of the bottom wall

θ_i dimensionless temperature of the vertical walls

References

- [1] D. Angirasa, G.P. Peterson, Natural convection heat transfer from an isothermal vertical surface to a fluid saturated thermally stratified porous medium, International Journal of Heat and Mass Transfer, 40(18) (1997) 4329-4335.
- [2] C.C. Chen, R. Eichhorn, Natural convection from a vertical surface to a thermally stratified fluid, Journal of Heat Transfer, 98(3) (1976) 446-451.
- [3] R.K. Tripathi, G. Nath, Unsteady natural convection flow over a vertical plate embedded in a stratified medium, International Journal of Heat and Mass Transfer, 36(4) (1993) 1125-1128.
- [4] M.M. Rahaman, S. Bhowmick, S. C. Saha, Unsteady Natural Convection and Entropy Generation in Thermally Stratified Trapezoidal Cavities: A Comparative Study, Processes, 13(6) (2025) 1908.
- [5] M.M. Rahaman, S. Bhowmick, R.N. Mondal, S.C. Saha, A computational study of chaotic flow and heat transfer within a trapezoidal cavity, Energies, 16(13) (2023)

5031.

[6] S. Bhowmick, S.C. Saha, M. Qiao, F. Xu, Transition to a chaotic flow in a V-shaped triangular cavity heated from below, *International Journal of Heat and Mass Transfer*, 128 (2019) 76-86.

[7] X. Wang, S. Bhowmick, Z.F. Tian, S.C. Saha, F. Xu, Experimental study of natural convection in a V-shape-section cavity, *Physics of Fluids*, 33(1) (2021) 014104.

[8] J. Patterson, J. Imberger, J. Unsteady natural convection in a rectangular cavity, *Journal of Fluid Mechanics*, 100(1) (1980) 65-86.

[9] T.S. Lee, Numerical experiments with fluid convection in tilted nonrectangular enclosures, *Numerical Heat Transfer*, 19(4) (1991), 487-499.

[10] J. Ma, F. Xu, Unsteady natural convection and heat transfer in a differentially heated cavity with a fin for high Rayleigh numbers, *Applied Thermal Engineering*, 99 (2016) 625-634.

[11] Y. Varol, H.F. Oztop, I. Pop, Numerical analysis of natural convection for a porous rectangular enclosure with sinusoidally varying temperature profile on the bottom wall, *International Communications in Heat and Mass Transfer*, 35(1) (2008) 56-64.

[12] S.C. Saha, Unsteady natural convection in a triangular enclosure under isothermal heating, *Energy and Buildings*, 43(2-3) (2011) 695-703.

[13] M. Bouafia, O. Daube, Natural convection for large temperature gradients around a square solid body within a rectangular cavity, *International Journal of Heat and Mass Transfer*, 50(17-18) (2007) 3599-3615.

[14] F. Xu, J.C. Patterson, C. Lei, Unsteady flow and heat transfer adjacent to the sidewall wall of a differentially heated cavity with a conducting and an adiabatic fin, *International Journal of Heat and Fluid Flow*, 32(3) (2011) 680-687.

[15] L. Iyican, L.C. Witte, Y. Bayazitoglu, An experimental study of natural convection in trapezoidal enclosures, *Journal of Heat Transfer*, 102(4) (1980) 648-653.

[16] E. Natarajan, S. Roy, T. Basak, Effect of various thermal boundary conditions on natural convection in a trapezoidal cavity with linearly heated side wall (s), *Numerical Heat Transfer, Part B: Fundamentals*, 52(6) (2007) 551-568.

[17] M.M. Rahman, M.A. Hye, M.M. Rahman, M.M. Rahaman, Numerical simulation on MHD free convection mass and heat transfer fluid flow over a vertical porous plate in a rotating system with induced magnetic field, *Annals of Pure and Applied Mathematics*, 7(2) (2014) 35-44.

[18] G. De Vahl Davis, Natural convection of air in a square cavity: a bench mark numerical solution, *International Journal for Numerical Methods in Fluids*, 3(3) (1983) 249-264.

[19] T. Basak, S. Roy, A.R. Balakrishnan, Effects of thermal boundary conditions on natural convection flows within a square cavity, *International Journal of Heat and Mass Transfer*, 49(23-24) (2006) 4525-4535.

[20] A. Raji, M. Hasnaoui, M. Firdaouss, C. Ouardi, Natural convection heat transfer enhancement in a square cavity periodically cooled from above, *Numerical Heat Transfer, Part A: Applications*, 63(7) (2013) 511-533.

[21] T. Pesso, S. Piva, Laminar natural convection in a square cavity: low Prandtl numbers and large density differences, *International Journal of Heat and Mass Transfer*, 52(3-4) (2009) 1036-1043.

[22] I. Kouroudis, P. Saliakellis, S.G. Yiantsios, Direct numerical simulation of natural convection in a square cavity with uniform heat fluxes at the vertical sides: Flow structure and transition, *International Journal of Heat and Mass Transfer*, 115 (2017) 428-438.

[23] Q.H. Deng, Fluid flow and heat transfer characteristics of natural convection in square cavities due to discrete source-sink pairs, *International Journal of Heat and Mass Transfer*, 51(25-26) (2008) 5949-5957.

[24] G. Barakos, E. Mitsoulis, D.O. Assimacopoulos, Natural convection flow in a square cavity revisited: laminar and turbulent models with wall functions, *International Journal for Numerical Methods in Fluids*, 18(7) (1994) 695-719.

[25] S.A. Bawazeer, M.S. Alsoufi, Natural Convection in a Square Cavity: Effects of Rayleigh and Prandtl Numbers on Heat Transfer and Flow Patterns, *Case Studies in Thermal Engineering*, 73 (2025) 106680.

[26] A. Bejan, Entropy generation minimization: The new thermodynamics of finite-size devices and finite-time processes, *Journal of Applied Physics*, 79(3) (1996) 1191-1218.

[27] P. Biswal, T. Basak, Entropy generation based approach on natural convection in enclosures with concave/convex side walls, *International Journal of Heat and Mass Transfer*, 82 (2015) 213-235.

[28] M. Bouabid, M. Magherbi, N. Hidouri, A.B. Brahim, Entropy generation at natural convection in an inclined rectangular cavity, *Entropy*, 13(5) (2011) 1020-1033.

[29] R.D.C. Oliveski, M.H. Macagnan, J.B. Copetti, Entropy generation and natural convection in rectangular cavities, *Applied Thermal Engineering*, 29(8-9) (2009) 1417-1425.

[30] M.M. Rahaman, S. Bhowmick, G. Saha, F. Xu, S.C. Saha, Transition to chaotic flow, bifurcation, and entropy generation analysis inside a stratified trapezoidal enclosure for varying aspect ratio, *Chinese Journal of Physics*, 91 (2024) 867-882.

[31] M.M. Rahaman, S. Bhowmick, S.C. Saha, Thermal Performance and Entropy Generation of Unsteady Natural Convection in a Trapezoid-Shaped Cavity, *Processes*, 13(3) (2025) 921.

[32] A.K. Singh, S. Roy, T. Basak, Analysis of entropy generation due to natural convection in tilted square

cavities, Industrial & Engineering Chemistry Research, 51(40) (2012) 13300-13318.

[33] G.G. Ilis, M. Mobedi, B. Sunden, Effect of aspect ratio on entropy generation in a rectangular cavity with differentially heated vertical walls, International Communications in Heat and Mass Transfer, 35(6) (2008) 696-703.

[34] M.A. Sheremet, T. Grosan, I. Pop, Natural convection and entropy generation in a square cavity with variable temperature side walls filled with a nanofluid: Buongiorno's mathematical model, Entropy, 19(7) (2017) 337.

[35] J.H. Saboj, P. Nag, G. Saha, S.C. Saha, Entropy production analysis in an octagonal cavity with an inner cold cylinder: a thermodynamic aspect, Energies, 16(14) (2023) 5487.

[36] S.M. Shavik, M.N. Hassan, A.M. Morshed, M.Q. Islam, Natural convection and entropy generation in a square inclined cavity with differentially heated vertical walls, Procedia Engineering, 90 (2014) 557-562.

[37] M.M. Rahaman, S. Bhowmick, R.N. Mondal, S.C. Saha, Unsteady natural convection in an initially stratified air-filled trapezoidal enclosure heated from below, Processes, 10(7) (2022) 1383.

[38] M.M. Rahaman, S. Bhowmick, B.P. Ghosh, F. Xu, R.N. Mondal, S.C. Saha, Transient natural convection flows and heat transfer in a thermally stratified air-filled trapezoidal cavity, Thermal Science and Engineering Progress, 47 (2024) 102377.

[39] S. Bhowmick, F. Xu, M.M. Molla, S.C. Saha, Chaotic phenomena of natural convection for water in a V-shaped enclosure, International Journal of Thermal Sciences, 176 (2022) 107526.

[40] S. Bhowmick, S.C. Saha, M. Qiao, F. Xu, Transition to a chaotic flow in a V-shaped triangular cavity heated from below, International Journal of Heat and Mass Transfer, 128, (2019) 76-86.

HOW TO CITE THIS ARTICLE

Md. N. Hossain, S. M. Hassan Shaon, Md. M. Rahaman, Transient Natural Convection and Entropy Generation Analysis in a Stratified Square Enclosure, AUT J. Mech Eng., 10(2) (2026) 153-166.

DOI: [10.22060/ajme.2025.24319.6190](https://doi.org/10.22060/ajme.2025.24319.6190)

